Biochimica et Biophysica Acta 1848 (2015) 434–443

Contents lists available at ScienceDirect

Biochimica et Biophysica Acta

journal homepage: www.elsevier.com/locate/bbamem

Effect of glycyrrhetinic acid on lipid raft model at the air/water interface

Seiichi Sakamoto [a,*], Takuhiro Uto [b], Yukihiro Shoyama [b]

[a] Department of Pharmacognosy, Graduate School of Pharmaceutical Sciences, Kyushu University, 3-1-1 Maidashi, Higashi-ku, Fukuoka 812–8582, Japan
[b] Department of Pharmacognosy, Faculty of Pharmaceutical Sciences, Nagasaki International University, 2825-7 Huis Ten Bosch, Sasebo, Nagasaki 859-3298, Japan

ARTICLE INFO

Article history:
Received 18 September 2014
Received in revised form 24 October 2014
Accepted 13 November 2014
Available online 20 November 2014

Keywords:
Glycyrrhetinic acid (GA)
Glycyrrhizin (GC)
Langmuir monolayer
Lipid raft
Membrane-disrupting activity

ABSTRACT

To investigate an interfacial behavior of the aglycon of glycyrrhizin (GC), glycyrrhetinic acid (GA), with a lipid raft model consisting of equimolar ternary mixtures of *N*-palmitoyl sphingomyelin (PSM), dioleoylphosphatidylcholine (DOPC), and cholesterol (CHOL), Langmuir monolayer techniques were systematically conducted. Surface pressure (π)–molecular area (A) and surface potential (ΔV)–A isotherms showed that the adsorbed GA at the air/water interface was desorbed into the bulk upon compression of the lipid monolayer. In situ morphological analysis by Brewster angle microscopy and fluorescence microscopy revealed that the raft domains became smaller as the concentrations of GA in the subphase (C_{GA}) increased, suggesting that GA promotes the formation of fluid networks related to various cellular processes via lipid rafts. In addition, ex situ morphological analysis by atomic force microscopy revealed that GA interacts with lipid raft by lying down at the surface. Interestingly, the distinctive striped regions were formed at $C_{GA} = 5.0$ μM. This phenomenon was observed to be induced by the interaction of CHOL with adsorbed GA and is involved in the membrane-disrupting activity of saponin and its aglycon. A quantitative comparison of GA with GC (Sakamoto et al., 2013) revealed that GA interacts more strongly with the raft model than GC in the monolayer state. Various biological activities of GA are known to be stronger than those of GC. This fact allows us to hypothesize that differences in the interactions of GA/GC with the model monolayer correlate to their degree of exertion for numerous activities.

1. Introduction

The root and stolon of the genus *Glycyrrhiza* (licorice) are the most frequently used natural resources in Japanese traditional Kampo medicines and are known to exhibit various pharmacological activities, including hepatoprotective [1,2], anti-*Helicobacter pylori* [3], anti-inflammatory [4,5], anti-ulcer [6], expectorant [7], anti-microbial [8–10], and memory enhancing [11] activities. Because of its outstanding activities, more than 70% of prescribed Kampo medicines contain licorice. In addition, licorice has also been used worldwide as a sweetener, tobacco flavoring agent, and food additive. In addition, it is used in cosmetics and confectionery foods [12]; therefore, it was recently selected as the "Medicinal plant of the year 2012" by the University of Würzburg, WWF, TRAFFIC. The major bioactive compound of licorice is glycyrrhizin (GC), which is structurally classified as an oleanane-type triterpenoid saponin that possesses two glucuronic acid groups in a molecule. Because GC is metabolized to glycyrrhetinic acid (GA; Fig. 1) by human intestinal flora after being administered orally [13], GA, rather than GC, is expected to be the active form that exerts numerous biological activities. Indeed, GA as well as GC have been reported to have a large number of biological activities, which include anti-estrogenic [14], anti-inflammatory [15], anti-ulcer [16], anti-asthmatic [17], inhibitory activity of human complement [18] and 11β-hydroxysteroid dehydrogenase type 2 (11βHSD2) [19], and anti-viral activity [20,21]. In addition, GA has been shown to exhibit various anti-tumor activities against leukemia cells [22], the human hepatoma cell line HepG2 [23,24], breast cancer cell lines MCF-7 and ZR-75-1 [23,25,26], and androgen-dependent prostate cancer cell line LNCaP [27]. Recently, fitting analysis by a molecular modeling method of various triterpenoids to 11βHSD2 was performed to predict the toxic effects of triterpenoids on tumor cells by 11βHSD2 inhibition. This study revealed that GA was the best-fitted triterpenoid to the ligand binding site in 11βHSD2, which led to the apoptosis of the tumor cells [28].

Microdomains enriched in sphingolipids (sphingomyelin (SM) and glycosphingolipids) and cholesterol (CHOL) have recently been a subject of great interest in cell biology because they provide dynamic scaffolding for a variety of different and crucial cellular processes including protein trafficking [29], signal transduction [30,31], CHOL and membrane transport [32–34], and calcium homeostasis [35]. The long saturated acyl chains in sphingolipids are thought to strongly interact with CHOL to form a liquid-ordered (l_o) phase, whereas unsaturated phospholipids are loosely packed to form a liquid-disordered (l_d) phase [36–39]. These different properties in packing states induce phase separation to organize microdomains so-called lipid rafts [40]. So far, numerous studies related to the organization of lipid rafts have been physicochemically conducted by using lipid mixtures that mimic the components of the outer leaflets of plasma membranes, where the

* Corresponding author. Tel./fax: +81 92 642 6581.
E-mail address: s.sakamoto@phar.kyushu-u.ac.jp (S. Sakamoto).

http://dx.doi.org/10.1016/j.bbamem.2014.11.014
0005-2736/

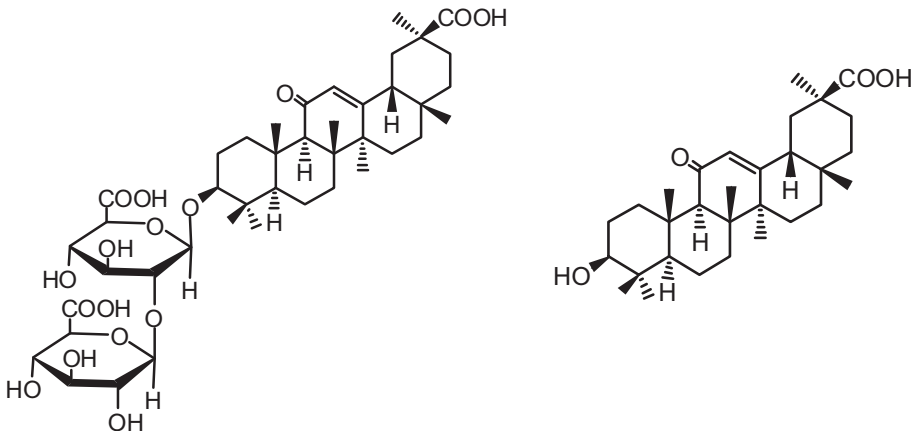

Glycyrrhizin (GC) Glycyrrhetinic acid(GA)

Fig. 1. Structures of glycyrrhizin (GC) and glycyrrhetinic acid (GA).

combination of sphingolipids, phospholipids, and CHOL has been most widely utilized. To directly address the lateral organization of lipid rafts, the Langmuir monolayer and Langmuir–Blodgett (LB) techniques, atomic force microscopy (AFM) [41–44], Brewster angle microscopy (BAM) [45,46], and fluorescence microscopy (FM) [47–54] have been used to investigate the raft-mimicking lipid mixtures. In particular, the Langmuir monolayer behavior during compression and expansion well reproduces dynamic formation and destruction of the lipid rafts. These methods enable us to visually provide information regarding the phase variations (or lateral diffusion) on micro- and nano-scales.

In a previous study, the interfacial behavior of GC with a lipid raft model of equimolar ternary *N*-palmitoyl sphingomyelin (PSM), dioleoylphosphatidylcholine (DOPC), and CHOL monolayers has been systematically explored [55]. GC was observed to regulate the size of the raft domains by interacting from the bulk to increase a liquid-expanded (LE) network, which is considered to play an important role in the substance transportation via lipid rafts. Moreover, GC-derived distinctive stripped regions resembling the feature of membrane disruption so-called hemolytic activity were successfully observed at a GC concentration of 50 μM in the subphase (C_{GC} = 50 μM), despite the fact that the degree of GC's hemolytic activity is relatively low.

Here, we investigated the interaction of GA, which is the hydrolysate of GC by human intestinal flora, with the equimolar ternary PSM/DOPC/CHOL monolayer to gain insight into the interfacial behavior of raft domains in the presence of GA. GA was dissolved in the subphase solution, where the pH and ionic strength were adjusted to physiological conditions, to clarify the interaction of adsorbed GA from the bulk with the raft model. Moreover, in this study, AFM observation was conducted to visually investigate the interaction manner between GA and the lipid raft model at the air/water interface. By comparing the interfacial behaviors of GA with those of GC described in our previous study [55], the effect of glucuronic acid groups on the lipid raft model and hemolytic activity were also discussed.

2. Materials and methods

2.1. Materials

Glycyrrhetinic acid (GA; ≥99%) was obtained from Nagara Science Co. (Gifu, Japan). *N*-Palmitoyl-D-*erythro*-sphingosylphosphorylcholine (*N*-palmitoyl sphingomyelin, PSM; >99%), 1,2-dioleoyl-*sn*-glycero-3-phosphocholine (dioleoylphosphatidylcholine, DOPC; >99%), and 1-palmitoyl-2-{6-[(7-nitro-2-1,3-benzoxadiazol-4-yl)amino]hexanoyl}-*sn*-glycero-3-phosphocholine (NBD-PC; >99%) were purchased from Avanti Polar Lipids (Alabaster, AL, USA). Cholesterol (CHOL; ≥99%) was obtained from Sigma Chemical Co. (St. Louis, MO, USA). These lipids and GA were used without further purification. Chloroform (99.7%) and methanol (99.8%), which were used as spreading solvents, were purchased from Kanto Chemical Co. (Tokyo, Japan) and Nacalai Tesque (Kyoto, Japan), respectively. The chloroform/methanol (2/1, v/v) mixture was used for the preparation of stock solutions of PSM (0.5 mM), DOPC (0.5 mM), and CHOL (1.0 mM) monolayers. Tris(hydroxymethyl) aminomethane (Tris), NaCl, and acetic acid were obtained from Nacalai Tesque. NaCl was heated at 1023 K for 24 h before use to remove all surface-active organic impurities. Triply distilled water (surface tension = 72.0 mN m^{-1} at 298.2 K and the electrical resistivity = 18 MΩ cm) was used for the preparation of the subphase solution.

2.2. Surface pressure–area isotherms

The surface pressure (π) of Langmuir monolayers was measured with an automated homemade Wilhelmy balance (Mettler Toledo, AG-245) with a surface pressure resolution of 0.01 mN m^{-1}. The pressure-measuring system was equipped with a filter paper (Whatman 541, periphery = 4 cm). The trough was made from Teflon-coated brass (area = 750 cm^2), and both hydrophobic and lipophobic Teflon barriers were used in this study. π–molecular area (A) isotherms were recorded at a temperature of 298.2 ± 0.1 K, which was thermostatically controlled by a circulating water system. After the sample was spread onto the surface, monolayers were allowed to compress for 15 min to evaporate the spreading solvent. The monolayer was compressed at a speed of ~0.10 nm^2 per molecule per minute. Standard deviations (SD) for A and π were ~0.01 nm^2 and ~0.1 mN m^{-1}, respectively. The subphase was prepared at 0.02 M Tris buffer with 0.13 M NaCl containing different concentrations of GA. Its pH was adjusted to 7.4 with an adequate volume of acetic acid.

2.3. Surface potential–area isotherms

The measurement of surface potential (ΔV) was performed simultaneously with the π measurement when the monolayer was compressed at the air/water interface. It was monitored using ionizing an ^{241}Am electrode placed 1–2 mm above the interface while a reference electrode was dipped into the subphase. An electrometer (Keithley 614) was used to measure the ΔV. The SD for ΔV was ~5 mV.

2.4. Surface tension measurements

The surface tension (γ) of GA solutions was determined at 298.2 K by using a drop volume tensiometer (YHC-2010, YTS, Japan) [55], which measures the volume of a drop detaching from a capillary with known diameter. Temperature was controlled within ± 0.01 K by means of a thermostat. The SD for γ was ~0.05 mN m^{-1}.

2.5. Brewster angle microscopy

The monolayer was directly visualized by a Brewster angle microscope (BAM; KSV Optrel BAM 300, KSV Instruments, Finland) coupled to a commercially available film balance system (KSV Minitrough, KSV Instruments, Finland) at 298.2 ± 0.1 K. In the BAM experiments, a 20 mW He–Ne laser was used as light source at the wavelength of 632.8 nm. A Glan–Thompson polarizer placed between laser and minitrough provided *p*-polarized light at the Brewster angle (53.1° from vertical for a pure water surface). A 10× objective lens allowed a lateral resolution of ~2 μm. The angle of the incident beam to the air/water interface was fixed to the Brewster angle, and the reflected beam was recorded with a high grade charge coupled device (CCD) camera (EHDkamPro02, EHD Imaging GmbH, Germany). The BAM images were digitally saved on the computer hard disk.

2.6. Fluorescence microscopy

The film balance system (KSV Minitrough, KSV Instruments, Finland) was mounted onto the stage of an Olympus BX51W1 microscope (Tokyo, Japan) equipped with a 100 W mercury lamp (USH-1030L), an objective lens (SLMPlan 50×, working distance = 15 mm), and a 3CCD camera control unit (IKTU51CU, Toshiba, Japan). The samples for fluorescence microscopy (FM) were prepared by the addition of 1 mol% of the phospholipid fluorescent probe, NBD-PC to the stock solution individually. The images observed at an excitation wavelength of 460 nm and an emission wavelength of 534 nm were directly recorded with the hard disk via an online image processor (DVgate Plus; Sony, Tokyo, Japan) connected to the microscope. Imaging processing and analysis were done using the software, Adobe Photoshop Elements ver. 9.0 (Adobe System Incorporated, CA). The total amount of ordered domains (dark contrast regions) was evaluated and expressed as a percentage per frame by dividing the respective frame into dark and bright regions.

2.7. Atomic force microscopy

The LB films were prepared using the KSV Minitrough. Freshly cleaved mica (Okenshoji Co., Tokyo, Japan) was coated with dimethyl polysiloxane (Fuji Systems Co., Tokyo, Japan) to make the mica's surface hydrophobic. Films were deposited by horizontally contacting siliconized-mica to the hydrophobic part of the monolayers at the air/water interface (a horizontal lifting method). At selected surface pressures of 15 mN m^{-1}, a transfer velocity of 1 mm min^{-1} was used for the film-forming materials on 0.02 M Tris buffer with 0.13 M NaCl (pH 7.4) containing different concentrations of GA (C_{GA} = 0, 0.5, and 5.0 μM) and GC (C_{GC} = 5.0 and 50 μM). LB films prepared with a deposition rate of ~1 were used in the experiments. AFM experiments were performed in the air at room temperature. The AFM images were obtained using an SPA 400 instrument (Seiko Instruments Co., Chiba, Japan) at room temperature in tapping mode, which provided both topographical and phase contact images.

2.8. Fabrication of adsorbed GA layers from the subphase

Solutions of 0.02 M Tris buffer with 0.13 M NaCl (pH 7.4) and containing different concentrations of GA (0, 0.10, 0.25, 0.50, 1.0, and 5.0 μM) were prepared as subphases. After pouring the subphase into the trough, we waited until GA adsorption onto the surface attained an equilibrium state. Then, samples such as PSM, DOPC, CHOL, and their mixtures were spread onto the surface. Isotherm measurements and microscopic observations were conducted in the same manner as previously described. Because GA exhibits low solubility in aqueous solution, the pre-dissolved method was utilized instead of the injection method after the monolayers had spread. All of the *π–A* and *ΔV–A* isotherms shown herein were normalized using γ and ΔV measured individually (Fig. S1); i.e., a zero value of π or ΔV indicates a non-covered surface of 0.02 M Tris buffer solution with 0.13 M NaCl (pH 7.4) in the absence of GA. Details of the method used for the normalization are described in a previous study [55].

3. Results and discussion

3.1. π–A and ΔV–A measurements of GA with equimolar ternary PSM/DOPC/CHOL monolayer

π–A and *ΔV–A* isotherms of equimolar ternary PSM/DOPC/CHOL (1/1/1) monolayer with different concentrations of GA (C_{GA} = 0, 0.10, 0.25, 0.50, 1.0, and 5.0 μM) were primarily measured at 298.2 K (Fig. 2). GA was dissolved in the subphase of 0.02 M Tris buffer with

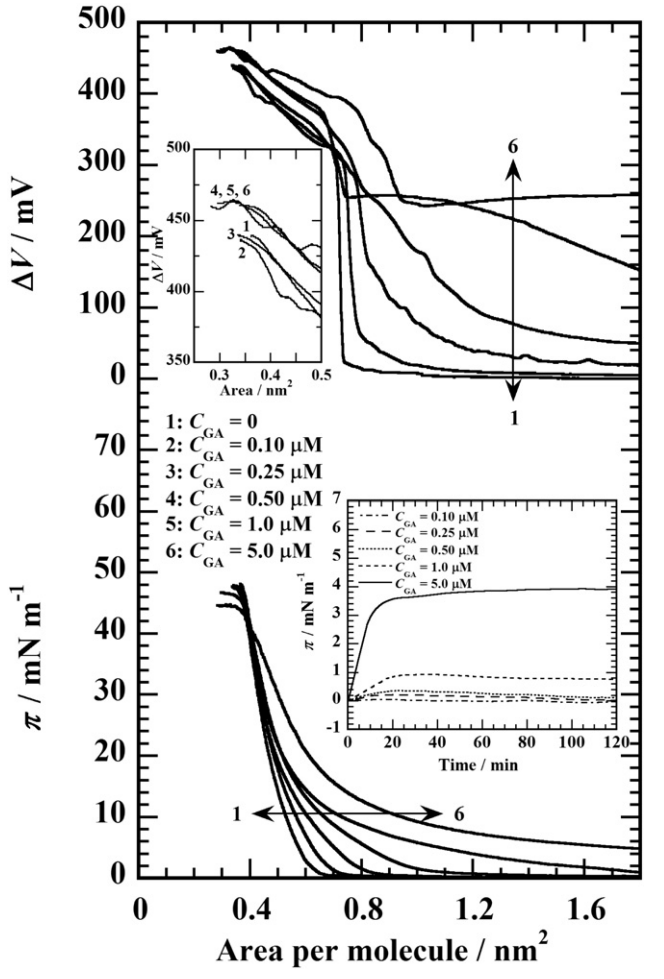

Fig. 2. The *π–A* and *ΔV–A* isotherms of the ternary PSM/DOPC/CHOL (1/1/1, by mol) monolayers on 0.02 M Tris buffer containing 0.13 M NaCl (pH 7.4) in the presence of different amounts of GA (C_{GA} = 0, 0.10, 0.25, 0.50, 1.0, and 5.0 μM) at 298.2 K. The inset at the upper-left represents enlarged *ΔV–A* isotherms in the surface potential region of 350 ≤ ΔV (in mV) ≤500, while the inset at the lower-right exhibits *π–t* isotherms for adsorption of GA from the subphases containing different C_{GA}. Note that the area axis means mean molecular area of the PSM/DOPC/CHOL mixtures, where molecular weight and amount of adsorbed GA are not considered.

0.13 M NaCl (pH 7.4), and then the subphase was poured into the trough. After the adsorption of GA, the surface entered an equilibrium state and the monolayer was spread onto it. The lower inset of Fig. 2 represents π–time (t) isotherms showing the time dependence of GA adsorption from the bulk as a function of C_{GA}. The equilibrium time (t^{eq}) of adsorption depends on the GA concentration in the subphase. As a result, GA attained adsorption equilibrium within 30 min at the five concentrations tested. Therefore, the PSM/DOPC/CHOL monolayers were spread after t^{eq} in the present study. The π–A isotherms expanded significantly as C_{GA} increases. The monolayer at $C_{GA} = 0$ collapses at ~47 mN m^{-1}, where monolayers begin to transform into bilayer and multilayer structures. The surface pressure of monolayer collapse (π^c) at $C_{GA} = 5.0$ μM is ~43 mN m^{-1}, where the area of monolayer collapse (A^c) was ~0.38 nm^2, although the π^c is ~45 mN m^{-1} (A^c = ~0.38 nm^2) over the range 0.10 μM ≤ C_{GA} ≤ 1.0 μM. On the basis of this fact, GA has a possibility to lower the stability of the PSM/DOPC/CHOL monolayers. In addition, the π–A isotherms at the collapse are overlapped in the whole range of C_{GA}. This result suggests that almost all the GA molecules adsorbed are squeezed out of the surface upon compression. Fig. 3 shows the π–A and ΔV–A isotherms of equimolar binary (PSM/DOPC (1/1), PSM/CHOL (1/1), and DOPC/CHOL (1/1)) and pure (PSM, DOPC, and CHOL) systems at a fixed concentration of $C_{GA} = 5.0$ μM. A decrease in π^c is observed in all the binary systems (Fig. 3(A)). On the other hand, as shown in Fig. 3(B), the adsorbed GA molecules reduce π^c of DOPC and CHOL monolayers. However, π^c (~57 mN m^{-1}) of PSM monolayers with GA is the same as that without GA. These results indicate that DOPC and/or CHOL monolayers are affected by the attractive interaction with GA at high surface pressures during the squeeze-out motion of GA into the bulk. Therefore, the attractive force of GA is considered to cause the decrease in π^c related to monolayer stability.

π–A isotherms for the binary systems (Fig. 3(A)) also reveal that the A^c of the binary PSM/DOPC (~0.49 nm^2) and DOPC/CHOL (~0.40 nm^2) monolayers at $C_{GA} = 5.0$ μM becomes slightly larger than those without GA, where the A^c is ~0.48 nm^2 and ~0.39 nm^2, respectively (Table 1).

Table 1
Collapse pressure (π^c), collapse area (A^c), and maximum surface potential (ΔV_{max}) at π^c of equimolar binary (PSM/DOPC, PSM/CHOL, and DOPC/CHOL) monolayers at $C_{GA} = 0$ and 5.0 μM.

System	π^c (mN m^{-1})	A^c (nm^2)	ΔV_{max} (mV)
PSM/DOPC	46.4	0.48	377
PSM/DOPC (C_{GA} = 5.0 μM)	43.5	0.49	390
PSM/CHOL	51.6	0.32	436
PSM/CHOL (C_{GA} = 5.0 μM)	47.1	0.32	446
DOPC/CHOL	43.6	0.39	437
DOPC/CHOL (C_{GA} = 5.0 μM)	42.6	0.40	449

However, the binary PSM/CHOL monolayers at $C_{GA} = 0$ and 5.0 μM exhibit the same area (A^c = ~0.32 nm^2). These results imply that DOPC helps maintain the adsorbed GA at the interface at high surface pressures because DOPC is mutually contained in the binary (PSM/DOPC and DOPC/CHOL) systems. Correspondingly, A^c of PSM (~0.36 nm^2) and CHOL (~0.34 nm^2) monolayers in the presence of GA exhibits the same A^c as those prepared in the absence of GA, whereas A^c of DOPC monolayers with GA (~0.60 nm^2) is larger than that of DOPC monolayers without GA (~0.54 nm^2) (Fig. 3(B)). These results indicate that adsorbed GA remains at the interface even upon compression in DOPC monolayers, although most adsorbed GA molecules are squeezed out into the bulk in the case of PSM and CHOL monolayers. Driving forces for the interaction between DOPC and GA are estimated to be primarily π–π bonding between the unsaturated acyl chains of DOPC and the double bond at the C-11 or C-12 position in the triterpenoid skeleton of GA and the similarities in the monolayer properties (i.e., liquid-expanded films) between the two.

ΔV values typically reflect the orientational and conformational variations of monolayers induced by compression. ΔV–A isotherms of the PSM/DOPC/CHOL monolayers show positive variations with

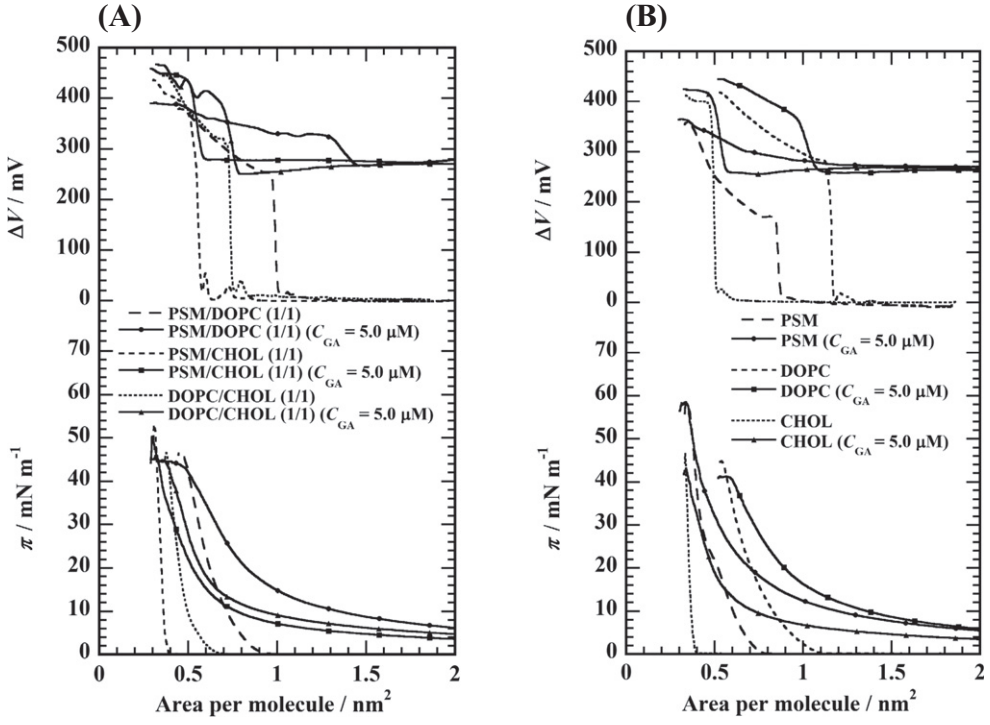

Fig. 3. The π–A and ΔV–A isotherms of (A) equimolar binary (PSM/DOPC, PSM/CHOL, and DOPC/CHOL) and (B) one-component (PSM, DOPC, and CHOL) systems on 0.02 M Tris buffer with 0.13 M NaCl (pH 7.4) at $C_{GA} = 5.0$ μM at 298.2 K. (A); Closed-circle, -square, and -triangle curves individually represent the curve of PSM/DOPC (1/1), PSM/CHOL (1/1), and DOPC/CHOL (1/1) in the presence of GA ($C_{GA} = 5.0$ μM). (B); Closed-circle, -square, and -triangle curves individually represent the curve of PSM, DOPC, and CHOL in the presence of GA ($C_{GA} = 5.0$ μM). Note that the area axis means mean molecular area of binary mixtures, where molecular weight and amount of adsorbed GA are not considered.

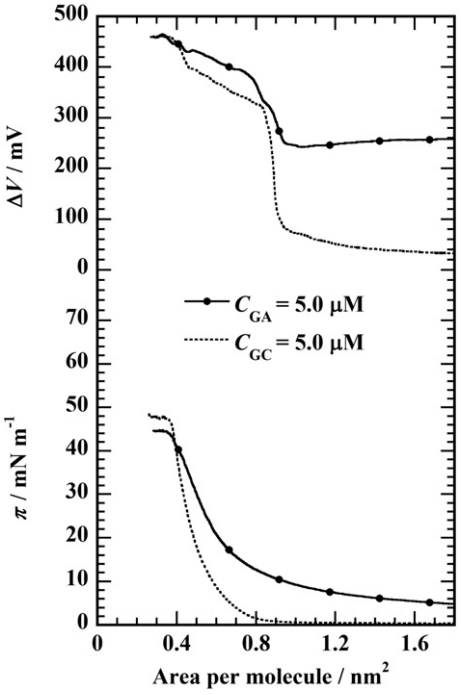

Fig. 4. The comparison of π–A and ΔV–A isotherms for ternary PSM/DOPC/CHOL (1/1/1; by mol) monolayers on 0.02 M Tris buffer with 0.13 M NaCl (pH 7.4) at C_{GA} and $C_{GC} = 5.0$ μM at 298.2 K.

decreasing molecular areas, suggesting that the monolayer orientation is improved in the direction normal to the surface plane [56,57]. Furthermore, maximum ΔV (ΔV_{max}) at 0.50 μM ≤ C_{GA} ≤ 5.0 μM (*curves* 4, 5, and 6) reach ~455 mV. This value is ~20 mV greater than that at 0 ≤ C_{GA} ≤ 0.25 μM (*curves* 1, 2, and 3). The difference in ΔV_{max} is attributed to the amount of GA left at the interface after being squeezed out. GA monolayers also have positive ΔV in both Langmuir monolayers (Fig. S2) and Gibbs monolayers (Fig. S1). When the amount of GA is small (C_{GA} = 0.10 and 0.25 μM), almost all the GA molecules are estimated to be located in the bulk below the PSM/DOPC/CHOL monolayers in the close-packed state because of a lack of contribution of GA to ΔV_{max}. However, when the amount of GA is large (0.50 μM ≤ C_{GA} ≤ 5.0 μM), GA molecules are assumed to remain just under the close-packed PSM/DOPC/CHOL monolayers, where the contribution of GA to ΔV_{max} values can be detected. Therefore, these different behaviors of GA molecules, which depend on GA concentration, are hypothesized to cause ΔV_{max} to differ by ~20 mV. Subsequently, we compared ΔV_{max} in the three equimolar binary (PSM/DOPC, PSM/CHOL, and DOPC/CHOL) systems with GA with those without GA (Fig. 3(A)). All ΔV_{max} in the systems with GA are larger than those in systems without GA (see Table 1). ΔV–A isotherms of pure individual monolayers account for this difference (Fig. 3(B)). ΔV_{max} of DOPC (~445 mV) and CHOL (~422 mV) monolayers with GA is larger than those without GA by ~25 mV. However, ΔV_{max} of PSM (~354 mV) monolayers at C_{GA} = 5.0 μM is the same as that of monolayers without GA. This fact suggests that the DOPC and CHOL monolayers contributed to an increase in ΔV_{max} by interacting with GA.

On the basis of π–A and ΔV–A isotherms of equimolar ternary, binary, and pure monolayers with and without GA, the interfacial behavior of individual components (PSM, DOPC, and CHOL) when they interact with GA (C_{GA} = 5.0 μM) under compression can be predicted. PSM monolayers squeeze out almost all the adsorbed GA molecules into the bulk upon compression, where the contribution of GA to ΔV is not detected. However, DOPC monolayers are absorbed to retain some adsorbed GA at the surface because ΔV_{max} and A^c increase by the remaining unabsorbed GA. In addition, the characteristics of DOPC and GA, which are similar to those of monolayers (LE phases), are attributed to keep adsorbed GA at the surface. With respect to CHOL monolayers, adsorbed GA is hypothesized to form a surface-associated aggregate just under the CHOL monolayer after being squeezed out of the surface [55]. This hypothesis can account for increase in ΔV_{max} and the lack of change in A^c, and is supported by the favorable interaction between CHOL and GA, which is induced by the structural resemblance of their sterol skeleton. CHOL has a hydroxyl group at the C-3 position, which can bind to two hydrophilic groups of GA through hydrogen bonding. Furthermore, the CHOL skeleton can attractively interact with the hydrophobic moiety of GA, its triterpenoid skeleton, through hydrophobic interactions.

Fig. 4 shows the π–A and ΔV–A isotherms of the ternary PSM/DOPC/CHOL monolayer at C_{GA} and C_{GC} = 5.0 μM [55]. π^c for the GA system (~43 mN m^{-1}) is lower than that for the GC system (~47 mN m^{-1}). Structural differences between GA and GC are two glucuronic acid groups. Thus, we hypothesize that the glucuronic acid groups cause the variation in π^c. In addition, the π–A isotherm for GA is expanded more than that for GC. Moreover, at A = 1.7 nm^2, initial π and ΔV of the GA system are higher than those of the GC system. These results suggest that the adsorbed GA molecule interacts with the PSM/DOPC/CHOL monolayer more strongly than GC, which is closely related to the fact that the GA exhibits stronger biological activities than GC at the same dose [21,58–60]. A comparison of π–A and ΔV–A isotherms between GA and GC allows us to postulate that interaction intensity against a membrane, which is based on surface activity, is involved in their exhibition of numerous activities. Correspondingly, a correlation between the membranes' toxicity toward saponins and their reduction in surface tension has been recently examined [61]. A strong correlation between these factors was observed; correlation coefficient was 0.94. Thus, the fact that the biological activities of GA and GC, which exert their activities (including anti-herpes virus type 1, anti-*H. pylori*, and anti-hepatotoxic activities) through membranes, exhibit a correlation with the surface activity of GA and GC. To address the correlation between the Langmuir monolayer model and the lipid raft model in the biological membrane in more detail, a bilayer study, such as a liposome study, is necessary. A comparison of the isotherms of GA and GC (Fig. 4) also reveals that π^c of the equimolar ternary monolayer at C_{GA} = 5.0 μM is lower than those at C_{GC} = 5 μM. That is, GA destabilizes the lipid raft to a greater extent than GC. We observed that the decrease in π^c is induced by DOPC and/or CHOL monolayers through an attractive interaction, as previously discussed. Therefore, the two glucuronic acid groups in GC are hypothesized to disrupt these interactions, resulting in higher π^c for GC than GA.

To further investigate the influence of GA on the equimolar ternary monolayer, a compressibility modulus (or dilatational elasticity modulus,

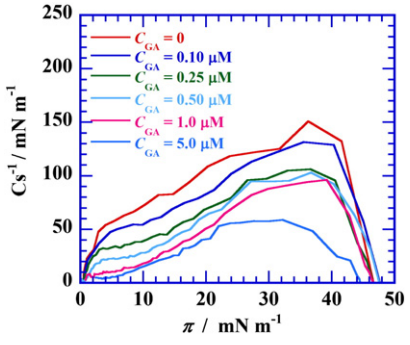

Fig. 5. Cs^{-1}–π curves of the ternary PSM/DOPC/CHOL (1/1/1, by mol) monolayers in the presence of different amounts of GA (C_{GA} = 0, 0.10, 0.25, 0.50, 1.0, and 5.0 μM). The compressibility (Cs^{-1}) values decrease as GA amounts increase, which suggests that the LE network is promoted by increasing the amount of GA.

Cs^{-1}) is calculated on the basis of π–A isotherms according to Eq. (1) [62]:

$$Cs^{-1} = -A\left(\frac{\partial \pi}{\partial A}\right)_T. \quad (1)$$

Cs^{-1} provides information related to the packed state of monolayers upon compression. A high compressibility modulus (or low compressibility) indicates a tight packing and a large cohesive force between the components. Fig. 5 shows Cs^{-1}–π curves of the ternary PSM/DOPC/CHOL monolayer in the presence of different concentrations of GA (C_{GA} = 0.10, 0.25, 0.50, 1.0, and 5.0 μM). Cs^{-1} decreases as C_{GA} increases, suggesting that the formation of LE phases is promoted by an increase in the amounts of GA. This result supports the study investigating the effect of GA on membrane fluidity by electron spin resonance, which indicated that GA significantly increases the lipid fluidity of plasma membranes [17].

3.2. Morphological observations of GA with equimolar ternary PSM/DOPC/CHOL monolayer using BAM, FM, and AFM

In situ morphological changes of the ternary PSM/DOPC/CHOL monolayer induced by the interaction with GA were investigated with BAM and FM. Fig. 6 shows the morphological images of the ternary monolayer as functions of π and C_{GA}. A fluorescent probe (here, NBD-PC) dissolves selectively into the LE phase in the monolayer state. Thus, the bright and dark contrasts in FM images correspond to LE (disordered) and liquid-condensed (LC; ordered) phases, respectively,

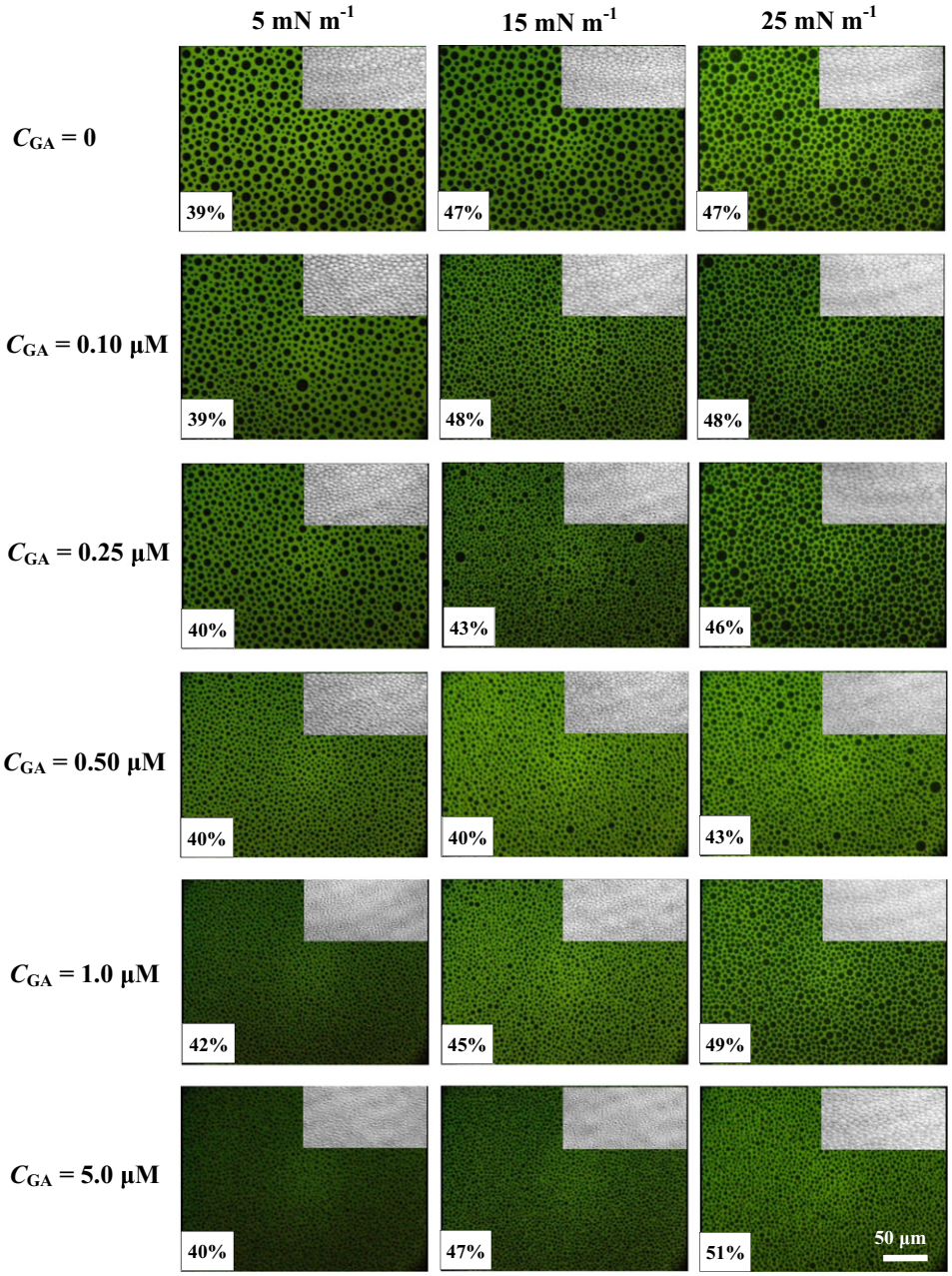

Fig. 6. Fluorescence micrographs of the ternary PSM/DOPC/CHOL (1/1/1, by mol) monolayers at three surface pressures (5, 15, and 25 mN m^{-1}) on 0.02 M Tris buffer with 0.13 M NaCl (pH 7.4) at C_{GA} = 0, 0.10, 0.25, 0.50, 1.0 and 5.0 μM at 298.2 K. The monolayers contain 1 mol% of the fluorescent probe (NBD-PC). The scale bars in the lower-right represent 50 μm. The corresponding BAM images are shown in the upper-right of each photograph. The percentages indicate the ration of occupied LC domains in the frame.

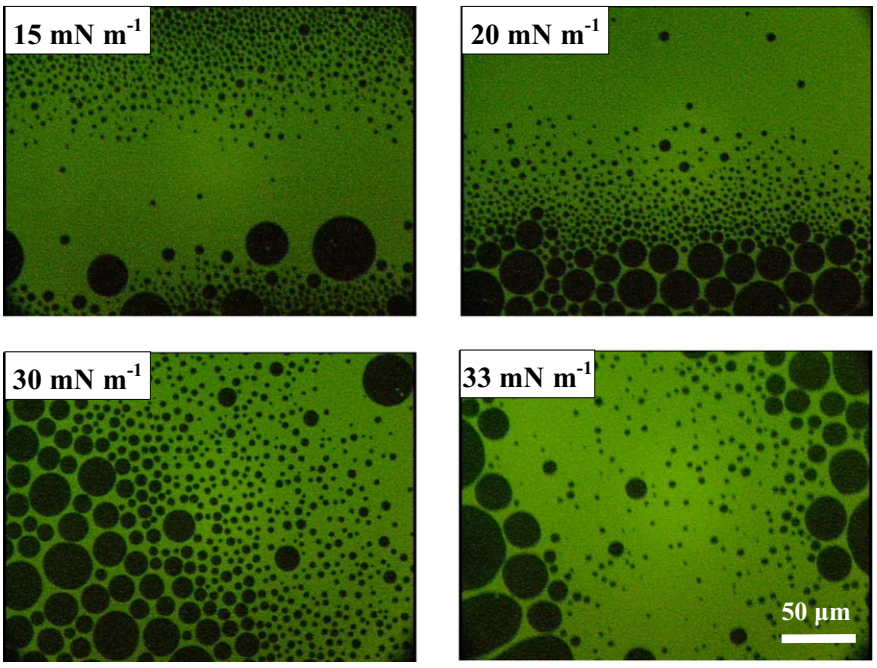

Fig. 7. Fluorescence micrographs of the ternary PSM/DOPC/CHOL (1/1/1, by mol) monolayers at four surface pressures (15, 20, 30, and 33 mN m^{-1}) on 0.02 M Tris buffer with 0.13 M NaCl (pH 7.4) at $C_{GA} = 5.0$ μM. The monolayers contain 1 mol% of the fluorescent probe (NBD-PC). The scale bar in the lower-right represents 50 μm. The distinctive striped GA regions are observed at $C_{GA} = 5.0$ μM in addition to the uniform raft domains seen in Fig. 6.

whereas the opposite contrasts are observed in BAM images. The images obtained from FM are well reproduced compared to those obtained from BAM, suggesting that the FM probe has little influence on the native morphology of the monolayers. Interestingly, FM and its corresponding BAM images indicate that the raft domains (dark contrast in FM images) become smaller as the percentage of retained LC

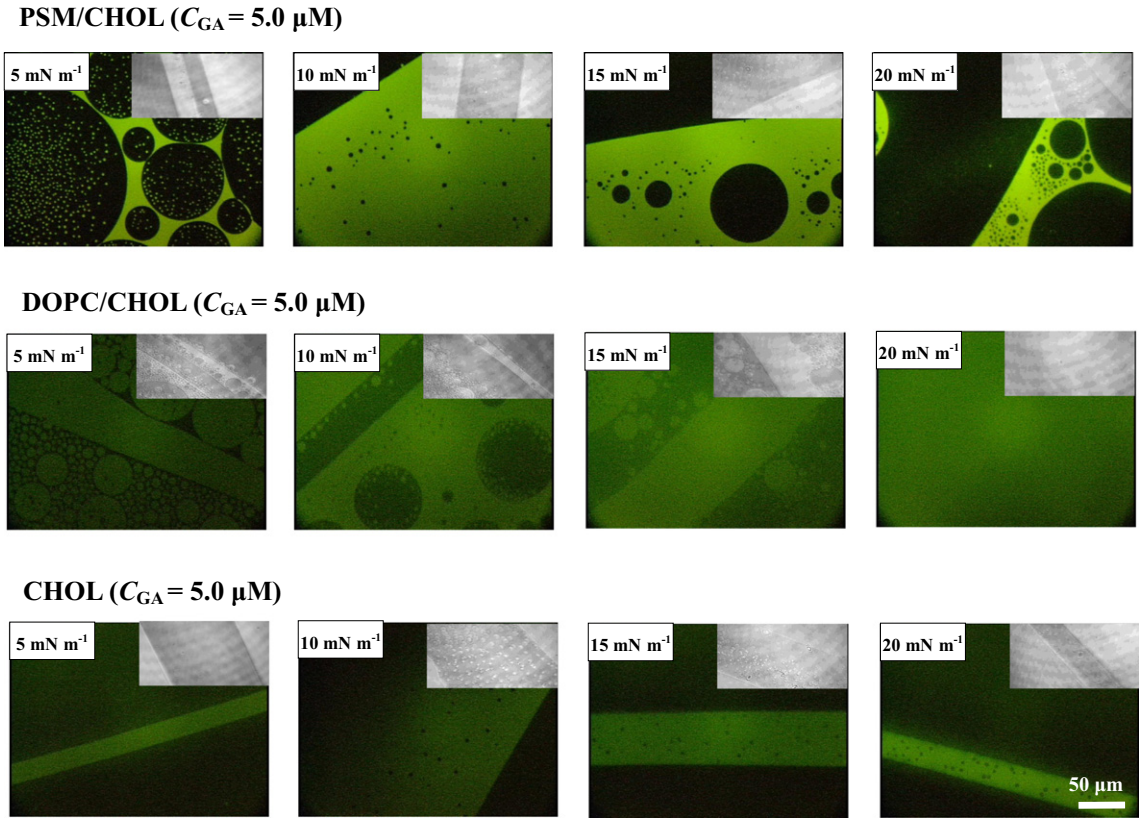

Fig. 8. Fluorescence micrographs of the equimolar binary (PSM/CHOL, and DOPC/CHOL) and pure CHOL monolayers at four various surface pressures (5, 10, 15, and 20 mN m^{-1}) on 0.02 M Tris buffer with 0.13 M NaCl (pH 7.4) at $C_{GA} = 5.0$ μM at 298.2 K. The monolayers contain 1 mol% of the fluorescent probe (NBD-PC). The scale bars in the lower-right represent 50 μm. The corresponding BAM images are shown in the upper-right of each photograph. CHOL was found to play an important role in forming distinctive striped regions, which is derived from GA.

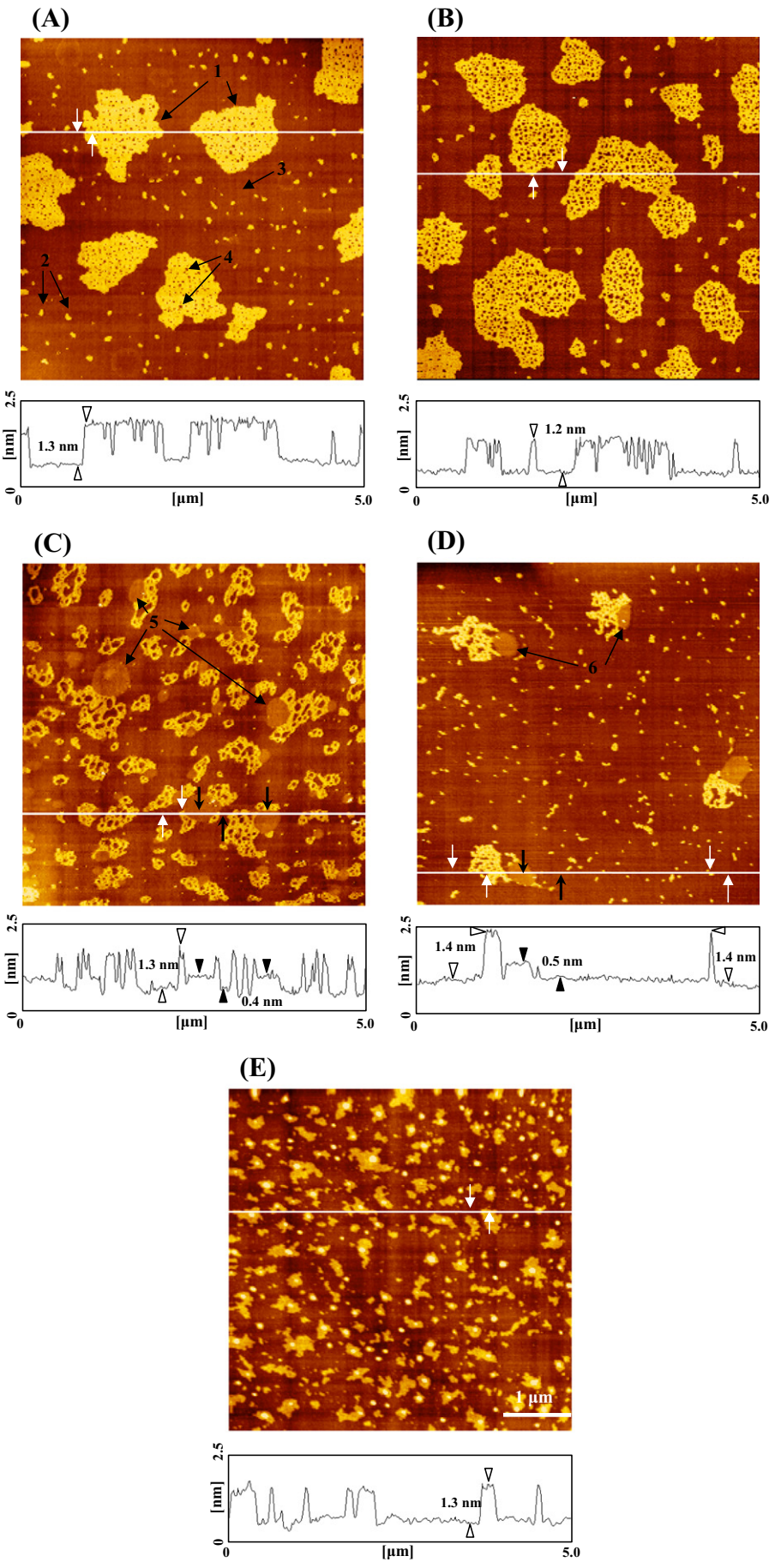
(A)
1
2
3
4
2.5
[nm]
0
1.3 nm
[µm]
5.0
(B)
1.2 nm
(C)
5
1.3 nm
0.4 nm
(D)
6
1.4 nm
0.5 nm
1.4 nm
(E)
1 µm

decreases, irrespective of an increase in C_{GA} from $C_{GA} = 0$ (top images) to 5.0 μM (bottom images) in Fig. 6. That is, CHOL-rich domains are finely dispersed by GA molecules. The distinctive striped GA regions are formed at $C_{GA} = 5.0$ μM in addition to the uniform raft domains (Fig. 7), which suggests that the uniform morphology of the ternary monolayer is separated by LE phases that are composed of adsorbed GA at the interface. This phenomenon is thought to be due to the excess amounts of adsorbed GA against LE regions of DOPC monolayers. In a previous study, similar striped regions derived from GC were observed at $C_{GC} = 50$ μM [55]. As a result, the phenomenon was speculated to be involved in the membrane-disrupting activity of GC, even though the degree of its activity is relatively low. GA is the aglycon moiety of GC, where the two glucuronic acid groups are eliminated by metabolism through β-glucuronidase produced from intestinal bacteria flora [13]. Therefore, GA is more hydrophobic than GC, resulting in the formation of distinctive striped regions at the lower GA concentration ($C_{GA} = 5.0$ μM) as compared with the case of GC ($C_{GC} = 50$ μM). With respect to the morphological analysis in the equimolar binary (PSM/DOPC (1/1), PSM/CHOL (1/1), and DOPC/CHOL (1/1)) and pure (PSM, DOPC, and CHOL) systems at $C_{GA} = 5.0$ μM, the distinctive striped GA regions (bright contrast) are observed only in PSM/CHOL, DOPC/CHOL, and CHOL systems (Fig. 8). These results suggest that the interaction between CHOL and GA causes such a phenomenon. The same phenomenon was observed when the equimolar ternary monolayer (PSM/DOPC/CHOL) was spread at $C_{GC} = 50$ μM, and CHOL was also the key component in the case of GC [55]. Recently, GA as well as GC have been reported to disrupt biological membranes [61]. Therefore, it is considerable that the GA-derived distinctive striped regions are deeply related to the membrane-disrupting activity of GA.

Ex situ morphological changes in the ternary monolayer were evaluated by using AFM to investigate raft behavior via interactions with GA. The horizontal resolution of the AFM images is poor, though the thickness resolution is excellent. Because AFM can discriminate nano-scale height differences between lipid domains, it is a suitable technique for studying raft domains [41–44]. The topological AFM images for the ternary monolayer at $C_{GA} = 0$, 0.5, and 5.0 μM are shown in Fig. 9(A–C). The film deposition was performed at a constant surface pressure of 15 mN m^{-1} because most GA molecules are squeezed out at high pressures, which makes the effect of GA difficult to detect in AFM images. In Fig. 9, the raft domains can be divided into 2 areas, where the bright (higher in height) raft domains (arrows 1), including surrounding small (arrows 2) and dark (lower in height) domains (arrow 3), are composed of a PSM–CHOL mixture and a PSM–DOPC mixture, respectively. Focusing on the surface of raft domains, a number of dark pinhole-like areas (arrows 4) are observed. Because the same morphology is evident in the AFM images of pure PSM films (Fig. S3), PSM is considered to be the major component that forms raft domains. As for the size, the raft domains become smaller within the range from ~1 to ~0.5 μm when C_{GA} increases from $C_{GA} =$ 0 to 5.0 μM, which corresponds to the BAM and FM images (Fig. 6), although the height differences remain constant (~1.3 nm) irrespective of C_{GA}. Interestingly, GA molecules were successfully observed at $C_{GA} = 5.0$ μM (arrows 5 in Fig. 9(C)) and were found to be located mostly beside the raft domains and on the surrounding dark domains. This result supports the π–A and ΔV–A isotherms that show that GA attractively interacts with CHOL and/or DOPC monolayers during squeeze-out motion. Fig. 9(D) and (E) displays AFM images for $C_{GC} = 5.0$ and 50 μM at 15 mN m^{-1}. Corresponding to the case of GA, the raft domains become smaller in size (from ~1 to ~0.3 μm) as C_{GC} increases. At $C_{GC} =$ 5.0 μM, GC molecules are observed just beside the raft domains (arrows 6 in Fig. 9(D)). Height differences between the raft domains and the GA/GC molecules are observed to be the same (~0.9 nm) without the effect of glucuronic acid groups (Fig. 9(C) and (D)), suggesting that both GA and GC molecules lie at the air/water interface through attachment of their hydrophilic groups to water molecules. However, the distinctive striped regions, which are observed at $C_{GA} = 5.0$ μM and $C_{GC} =$ 50 μM, are not identified in the narrow AFM scale.

4. Conclusion

The Langmuir monolayer technique was systematically employed to investigate the interfacial behavior of GA using a lipid raft model consisting of PSM, DOPC, and CHOL. π–A and ΔV–A isotherms and morphological observations revealed that GA regulates the size of raft domains below the monolayer to promote the formation of an LE state, which is considered to play an important role in the transportation of substances via lipid rafts. In addition, GA and GC molecules were observed to lie at the air/water interface while they interact with the lipid raft. The systematic monolayer study also revealed each interfacial behavior of the raft model components (PSM, DOPC, and CHOL) at high C_{GA}. Briefly, the PSM monolayer largely squeezes GA out of the interface into bulk, whereas the DOPC monolayer retains GA at the interface. CHOL monolayers also retain GA just under the monolayer after it has been squeezed out of the surface by forming a surface-associated aggregate. The results of this study indicate that the interaction of lipid rafts with GA is stronger than that with GC, which may be related to the greater biological activity of GA relative to that of GC. Since GA and its derivatives are widely used worldwide in drugs and cosmetics, the present findings provide useful information for estimating the three-dimensional interaction between a biomembrane and GA from the standpoint of health care.

Acknowledgements

The research in this paper was supported by The Japan Food Chemical Research Foundation. This work was also funded by a Grant-in-Aid for Young Scientists (B) [25750167] of the Japan Society for the Promotion of Science (JSPS). Finally, I thank O. Shibata for the discussion and H. Nakahara for the help with experiments, analyses, and comments on the manuscript.

Appendix A. Supplementary data

Surface tension (γ_{GA}) and surface potential (ΔV_{GA}) measurements of GA subphase ($C_{GA} = 0$, 0.10, 0.25, 0.50, 1.0, and 5.0 μM) for the base correction, the π–A and ΔV–A isotherms of insoluble GA monolayers spread on 5 M NaCl at 298.2 K, and AFM topographic image of pure PSM films at 25 mN m^{-1}. Supplementary data to this article can be found online at http://dx.doi.org/10.1016/j.bbamem.2014.11.014.

References

[1] C.V. Chandrasekaran, H.B. Deepak, H.P. Thiyagarajan, S. Kathiresan, G.K. Sangli, G.M. Deepak, A. Agarwal, Dual inhibitory effect of *Glycyrrhiza glabra* (GutGard™) on COX and LOX products, Phytomedicine 18 (2011) 278–284.
[2] J.R. Lee, S.J. Park, H.S. Lee, S.Y. Jee, J. Seo, Y.K. Kwon, T.K. Kwon, S.C. Kim, Hepatoprotective activity of licorice water extract against cadmium-induced toxicity in rats, Evid. Based Complement. Alternat. Med. 6 (2009) 195–201.
[3] T. Fukai, A. Marumo, K. Kaitou, T. Kanda, S. Terada, T. Nomura, Anti-*Helicobacter pylori* flavonoids from licorice extract, Life Sci. 71 (2002) 1449–1463.
[4] J.K. Kim, S.M. Oh, H.S. Kwon, Y.S. Oh, S.S. Lim, H.K. Shin, Anti-inflammatory effect of roasted licorice extracts on lipopolysaccharide-induced inflammatory responses in murine macrophages, Biochem. Biophys. Res. Commun. 345 (2006) 1215–1223.

Fig. 9. Typical AFM topographic images of the equimolar ternary PSM/DOPC/CHOL at (A) $C_{GA} = 0$, (B) 0.5, (C) 5.0 μM, (D) $C_{GC} = 5.0$ and (E) 50 μM at 15 mN m^{-1}. The scan area is 5.0 × 5.0 μm and the scale bar in the lower-right corner represents 1 μm. The cross-sectional profiles along the scanning line are shown just below the respective AFM images. The height difference between the arrows is indicated in the cross-sectional profile.

[5] S. Shibata, A drug over the millennia: pharmacognosy, chemistry, and pharmacology of licorice, Yakugaku Zasshi 120 (2000) 849–862.
[6] M. Mukherjee, N. Bhaskaran, R. Srinath, H.N. Shivaprasad, J.J. Allan, D. Shekhar, A. Agarwal, Anti-ulcer and antioxidant activity of GutGard, Indian J. Exp. Biol. 48 (2010) 269–274.
[7] H. Loosen, H. Kenter, *Glycyrrhiza* as an expectorant, Medizinische 43 (1955) 1520.
[8] A. Friis-Møller, M. Chen, K. Fuursted, S.B. Christensen, A. Kharazmi, *In vitro* antimycobacterial and antilegionella activity of licochalcone A from Chinese licorice roots, Planta Med. 68 (2002) 416–419.
[9] V.K. Gupta, A. Fatima, U. Faridi, A.S. Negi, K. Shanker, J.K. Kumar, N. Rahuja, S. Luqman, B.S. Sisodia, D. Saikia, M.P. Darokar, S.P.S. Khanuja, Antimicrobial potential of *Glycyrrhiza glabra* roots, J. Ethnopharmacol. 116 (2008) 377–380.
[10] W. Li, Y. Asada, T. Yoshikawa, Antimicrobial flavonoids from *Glycyrrhiza glabra* hairy root cultures, Planta Med. 64 (1998) 746–747.
[11] D. Dhingra, M. Parle, S.K. Kulkarni, Memory enhancing activity of *Glycyrrhiza glabra* in mice, J. Ethnopharmacol. 91 (2004) 361–365.
[12] H. Hayashi, H. Sudo, Economic importance of licorice, Plant Biotechnol. 26 (2009) 101–104.
[13] M. Hattori, T. Sakamoto, K. Kobashi, T. Namba, Metabolism of glycyrrhizin by human intestinal flora, Planta Med. 48 (1983) 38–42.
[14] S.D. Kraus, Glycyrrhetinic acid — a triterpene with antioestrogenic and anti-inflammatory activity, J. Pharm. Pharmacol. 12 (1960) 300–306.
[15] S. Amagaya, E. Sugishita, Y. Ogihara, S. Ogawa, K. Okada, T. Aizawa, Comparative studies of the stereoisomers of glycyrrhetinic acid on anti-inflammatory activities, J. Pharmacobiodyn. 7 (1984) 923–928.
[16] S. Yano, M. Harada, K. Watanabe, K. Nakamaru, Y. Hatakeyama, S. Shibata, K. Takahashi, T. Mori, K. Hirabayashi, M. Takeda, Antiulcer activities of glycyrrhetinic acid derivatives in experimental gastric lesion models, Chem. Pharm. Bull. 37 (1989) 2500–2504.
[17] Q. Shi, Y. Hou, J. Hou, P. Pan, Z. Liu, M. Jiang, J. Gao, G. Bai, Glycyrrhetic acid synergistically enhances β_2-adrenergic receptor-Gs signaling by changing the location of Gαs in lipid rafts, PLoS One 7 (2012) e44921.
[18] B.H. Kroes, C.J. Beukelman, A.J. van den Berg, G.J. Wolbink, H. van Dijk, R.P. Labadie, Inhibition of human complement by β-glycyrrhetinic acid, Immunology 90 (1997) 115–120.
[19] P.M. Stewart, A.M. Wallace, R. Valentino, D. Burt, C.H. Shackleton, C.R. Edwards, Mineralocorticoid activity of liquorice: 11-beta-hydroxysteroid dehydrogenase deficiency comes of age, Lancet 2 (1987) 821–824.
[20] M.E. Hardy, J.M. Hendricks, J.M. Paulson, N.R. Faunce, 18β-Glycyrrhetinic acid inhibits rotavirus replication in culture, Virol. J. 9 (2012) 96.
[21] T. Ikeda, K. Yokomizo, M. Okawa, R. Tsuchihashi, J. Kinjo, T. Nohara, M. Uyeda, Antiherpes virus type 1 activity of oleanane-type triterpenoids, Biol. Pharm. Bull. 28 (2005) 1779–1781.
[22] W. Logemann, F. Lauria, G. Cudkowicz, J. Franceschini, Antileukaemic activity of glycyrrhetinic acid, Nature 187 (1960) 607–608.
[23] T. Rossi, M. Castelli, G. Zandomeneghi, A. Ruberto, L. Benassi, C. Magnoni, S. Santachiara, G. Baggio, Selectivity of action of glycyrrhizin derivatives on the growth of MCF-7 and HEP-2 cells, Anticancer Res. 23 (2003) 3813–3818.
[24] Y. Satomi, H. Nishino, S. Shibata, Glycyrrhetinic acid and related compounds induce G1 arrest and apoptosis in human hepatocellular carcinoma HepG2, Anticancer Res. 25 (2005) 4043–4047.
[25] S. Hundertmark, H. Bühler, M. Rudolf, H.K. Weitzel, V. Ragosch, Inhibition of 11β-hydroxysteroid dehydrogenase activity enhances the antiproliferative effect of glucocorticosteroids on MCF-7 and ZR-75-1 breast cancer cells, J. Endocrinol. 155 (1997) 171–180.
[26] G. Sharma, S. Kar, S. Palit, P.K. Das, 18β-Glycyrrhetinic acid induces apoptosis through modulation of Akt/FOXO3a/Bim pathway in human breast cancer MCF-7 cells, J. Cell. Physiol. 227 (2012) 1923–1931.
[27] S. Hawthorne, S. Gallagher, Effects of glycyrrhetinic acid and liquorice extract on cell proliferation and prostate-specific antigen secretion in LNCaP prostate cancer cells, J. Pharm. Pharmacol. 60 (2008) 661–666.
[28] H. Yamaguchi, T. Yu, T. Noshita, Y. Kidachi, K. Kamiie, K. Yoshida, T. Akitaya, H. Umetsu, K. Ryoyama, Ligand–receptor interaction between triterpenoids and the 11β-hydroxysteroid dehydrogenase type 2 (11βHSD2) enzyme predicts their toxic effects against tumorigenic r/m HM-SFME-1 cells, J. Biol. Chem. 286 (2011) 36888–36898.
[29] K. Simons, E. Ikonen, Functional rafts in cell membranes, Nature 387 (1997) 569–572.
[30] S. Parpal, M. Karlsson, H. Thorn, P. Stralfors, Cholesterol depletion disrupts caveolae and insulin receptor signaling for metabolic control via insulin receptor substrate-1, but not for mitogen-activated protein kinase control, J. Biol. Chem. 276 (2001) 9670–9678.
[31] L.D. Zajchowski, S.M. Robbins, Lipid rafts and little caves. Compartmentalized signalling in membrane microdomains, Eur. J. Biochem. 269 (2002) 737–752.
[32] J.C. Holthuis, C. van Meer, K. Huitema, Lipid microdomains, lipid translocation and the organization of intracellular membrane transport (Review), Mol. Membr. Biol. 20 (2003) 231–241.
[33] K. Simons, D. Toomre, Lipid rafts and signal transduction, Nat. Rev. Mol. Cell Biol. 1 (2000) 31–39.
[34] E.J. Smart, Y. Ying, W.C. Donzell, R.G. Anderson, A role for caveolin in transport of cholesterol from endoplasmic reticulum to plasma membrane, J. Biol. Chem. 271 (1996) 29427–29435.
[35] S. Fedida-Metula, S. Elhyany, S. Tsory, S. Segal, M. Hershfinkel, I. Sekler, D. Fishman, Targeting lipid rafts inhibits protein kinase B by disrupting calcium homeostasis and attenuates malignant properties of melanoma cells, Carcinogenesis 29 (2008) 1546–1554.
[36] D.A. Brown, Seeing is believing: visualization of rafts in model membranes, Proc. Natl. Acad. Sci. 98 (2001) 10517–10518.
[37] J.H. Ipsen, G. Karlstrom, O.G. Mouritsen, H. Wennerstrom, M.J. Zuckermann, Phase equilibria in the phosphatidylcholine–cholesterol system, Biochim. Biophys. Acta 905 (1987) 162–172.
[38] D.J. Recktenwald, H.M. McConnell, Phase equilibria in binary mixtures of phosphatidylcholine and cholesterol, Biochemistry 20 (1981) 4505–4510.
[39] M.B. Sankaram, T.E. Thompson, Interaction of cholesterol with various glycerophospholipids and sphingomyelin, Biochemistry 29 (1990) 10670–10675.
[40] S. Munro, Lipid rafts: elusive or illusive? Cell 115 (2003) 377–388.
[41] J.C. Lawrence, D.E. Saslowsky, J. Michael Edwardson, R.M. Henderson, Real-time analysis of the effects of cholesterol on lipid raft behavior using atomic force microscopy, Biophys. J. 84 (2003) 1827–1832.
[42] N. Periasamy, H. Teichert, K. Weise, R.F. Vogel, R. Winter, Effects of temperature and pressure on the lateral organization of model membranes with functionally reconstituted multidrug transporter LmrA, Biochim. Biophys. Acta 1788 (2009) 390–401.
[43] H.A. Rinia, M.M.E. Snel, J.P.J.M. van der Eerden, B. de Kruijff, Visualizing detergent resistant domains in model membranes with atomic force microscopy, FEBS Lett. 501 (2001) 92–96.
[44] C. Yuan, J. Furlong, P. Burgos, L.J. Johnston, The size of lipid rafts: an atomic force microscopy study of ganglioside GM1 domains in sphingomyelin/DOPC/cholesterol membranes, Biophys. J. 82 (2002) 2526–2535.
[45] K. Hąc-Wydr, P. Dynarowicz-Łątka, P. Wydro, K. Bąk, Edelfosine disturbs the sphingomyelin–cholesterol model membrane system in a cholesterol-dependent way — the Langmuir monolayer study, Colloids Surf. B: Biointerfaces 88 (2011) 635–640.
[46] E. Prenner, G. Honsek, D. Hönig, D. Möbius, K. Lohner, Imaging of the domain organization in sphingomyelin and phosphatidylcholine monolayers, Chem. Phys. Lipids 145 (2007) 106–118.
[47] A. Radhakrishnan, H.M. McConnell, Cholesterol–phospholipid complexes in membranes, J. Am. Chem. Soc. 121 (1999) 486–487.
[48] K. Bacia, D. Scherfeld, N. Kahya, P. Schwille, Fluorescence correlation spectroscopy relates rafts in model and native membranes, Biophys. J. 87 (2004) 1034–1043.
[49] T. Baumgart, S.T. Hess, W.W. Webb, Imaging coexisting fluid domains in biomembrane models coupling curvature and line tension, Nature 425 (2003) 821–824.
[50] R.F.M. de Almeida, J. Borst, A. Fedorov, M. Prieto, A.J.W.G. Visser, Complexity of lipid domains and rafts in giant unilamellar vesicles revealed by combining imaging and microscopic and macroscopic time-resolved fluorescence, Biophys. J. 93 (2007) 539–553.
[51] J. Juhasz, F.J. Sharom, J.H. Davis, Quantitative characterization of coexisting phases in DOPC/DPPC/cholesterol mixtures: comparing confocal fluorescence microscopy and deuterium nuclear magnetic resonance, Biochim. Biophys. Acta 1788 (2009) 2541–2552.
[52] M.T. Stöckl, A. Herrmann, Detection of lipid domains in model and cell membranes by fluorescence lifetime imaging microscopy, Biochim. Biophys. Acta 1798 (2010) 1444–1456.
[53] S.L. Veatch, I.V. Polozov, K. Gawrisch, S.L. Keller, Liquid domains in vesicles investigated by NMR and fluorescence microscopy, Biophys. J. 86 (2004) 2910–2922.
[54] G. Wheeler, K.M. Tyler, Widefield microscopy for live imaging of lipid domains and membrane dynamics, Biochim. Biophys. Acta 180 (2011) 634–641.
[55] S. Sakamoto, H. Nakahara, T. Uto, Y. Shoyama, O. Shibata, Investigation of interfacial behavior of glycyrrhizin with lipid raft model via a Langmuir monolayer study, Biochim. Biophys. Acta 1828 (2013) 1271–1283.
[56] R. Maget-Dana, The monolayer technique: a potent tool for studying the interfacial properties of antimicrobial and membrane-lytic peptides and their interactions with lipid membranes, Biochim. Biophys. Acta 1462 (1999) 109–140.
[57] V. Vogel, D. Möbius, Local surface potentials and electric dipole moments of lipid monolayers: contributions of the water/lipid and the lipid/air interfaces, J. Colloid Interface Sci. 126 (1988) 408–420.
[58] R. Krausse, J. Bielenberg, W. Blaschek, U. Ullmann, *In vitro* anti-*Helicobacter pylori* activity of *Extractum liquiritiae*, glycyrrhizin and its metabolites, J. Antimicrob. Chemother. 54 (2004) 243–246.
[59] M. Nose, M. Ito, K. Kamimura, M. Shimizu, Y. Ogihara, A comparison of the antihepatotoxic activity between glycyrrhizin and glycyrrhetinic acid, Planta Med. 60 (1994) 136–139.
[60] Y. Yamamura, T. Santa, H. Kotani, K. Uchino, Y. Sawada, T. Iga, Administration-route dependency of absorption of glycyrrhizin in rats: intraperitoneal administration dramatically enhanced bioavailability, Biol. Pharm. Bull. 18 (1995) 337–341.
[61] S. Böttger, K. Hofmann, M.F. Melzig, Saponins can perturb biologic membranes and reduce the surface tension of aqueous solutions: a correlation? Bioorg. Med. Chem. 20 (2012) 2822–2828.
[62] J.T. Davies, E.K. Rideal, Interfacial Phenomena, 2nd ed. Academic Press, New York, 1963. 265.